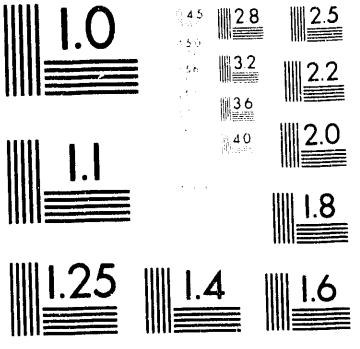
1.0
1.1
1.25
1.4
1.6
1.8
2.0
2.2
2.5
2.8
3.2
3.6
4.0
4.5
5.0

1 of 1

2

**METSAT, INC.**

515 South Howes • Fort Collins, CO 80521
Phone (303) 221-5420 • Fax (303) 493-3410

Specializing in METeorological SATellite Systems and Related Computer Technology



93-101

Final Report

to

University of California
Lawrence Livermore National Laboratory

for

Subcontract B208922
Under Prime Contract W-7405-ENG-48

for

# RAPTOR Transmissivity and Cloud Climatology Study

by

Kenneth E. Eis
Principal Investigator

With Contributions By:

Dr. Thomas H. Vonder Haar
John Forsythe
Takmeng Wong
Donald L. Reinke

January 1993

## DISCLAIMER

TABLE OF CONTENTS

## 1.0 INTRODUCTION

The RAPTOR Transmissivity Study (RTS) was funded by Lawrence Livermore National Laboratory (LLNL) under a sub contract to support the U.S. Army's RAPTOR program.

The intent of the study is to answer two questions stated in J.B.S Technologies Fax of 6-10-92:

1.1 What are the typical transmission levels of clouds as a function of target altitude for two locations and wavelengths of interest?

1.2 What fraction of time can we expect clouds to intervene with will reduce target signal below detection threshold levels (90% or 99% blockage of MWIR; any attenuation of SWIR) as a function of target altitude, wavelength, and the two geographic locations?

Answers to both questions are treated using existing software and data sources where possible due to the limited funding and scope of the contract.

## 2.0 METHODOLOGY

### 2.1 Transmissivity

The transmissivity question, as viewed from a meteorological perspective, can be partitioned into the transmissivity for the following regimes:

- Clear air transmissivity for low and high altitudes. Transmissivities for cloud-free regions are dependent upon aerosols and water vapor and are therefore temporally and regionally dependent.

- Low-level cloud transmissivity. Water vapor clouds in the lower regions of the atmosphere are characterized by exceptionally low transmissivities.

- High level cloud transmissivity. Ice crystal clouds, notably cirrus have a low transmissivity also but it is not as severe as the water clouds at lower altitudes.

- Sub-Visual Cirrus Clouds. These clouds have moderate transmissivities but will have to be treated independently from the other clouds because they are not observable (by definition) using conventional cloud detection means.

Transmissivity was calculated using the USAF MODTRAN version 7.0 This radiative transmission model calculates average transmittance, integrated absorption and the transmissivity at user-specified wavenumber intervals. The model contains cloud and sub-visual cirrus modules.

## 2.2 Cloud Obscuration Statistics

Question 2 can be posed as a probability as follows. What is the probability that a cloud will intervene between sensor and target for a given target altitude, range, wavelength and location? To answer this question METSAT used a high-resolution cloud data base extracted from GOES and GMS IR images and accumulated them over a month for a given universal time. This IR data was then converted into cloud/no cloud pixels. The cloud-designated pixels were then interrogated by using the IR radiance to establish a cloud-top temperature. Using a balloon sounding in the area of interest, a temperature vs. height relationship was established to provide the height of top and bottom for the interrogated volume. Each GOES pixel is 4 km x 8 km, while the GMS data is gridded into 10 km bins. The height of the volume is variable and based on the resolution of the balloon sounding data and the height of the modeled cloud. Figure 1 shows the interrogated volume and the geometry of the problem. Probabilities were determined by rotating about the sensor position, through all azimuth angles for each given target altitude, wavelength, range, and time combination.

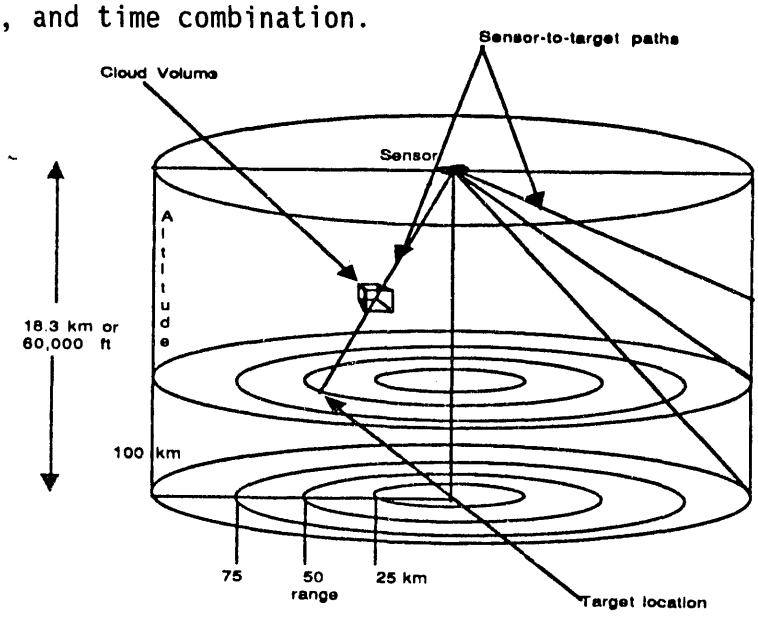


Figure 1. Interrogated volume and geometry of the problem.

## 3.0 DATA

### 3.1 Infrared Satellite Imagery

METSAT used available GOES-1 geostationary data from November 1979 for the Iraqi area of interest, and GMS geostationary satellite imagery for the cloud/no cloud information for the Korean area of interest. The 1979 year was selected from METSAT's extensive library of satellite imagery because it was the only period for which we had data over the Indian Ocean. In this position GOES-1 had a clear, low distortion view of the Iraq area. GMS data from 1979 through 1991 was available but, due to the limitations of the study, only the September 1984 data was analyzed.

### 3.2 Data Applicability to the Problem

Since only one month of data was used in the analysis for the Korean and Iraqi areas, the question of how representative this small sample is over a longer period of time is relevant. Figures 2 and 3 represent the cloud cover monthly means for the Iraq and Korean areas.

Figure 2 represents cloud data from the ISCCP database and the Nimbus satellite. This cloud data starts in April 1979 and represents the average cloud-cover value for the Iraq area box defined by 30 and 35 degrees north latitude, and 40 and 45 degrees east longitude. The November 1979 value represents a good average-to-cloudy cloud condition when compared to six years of mean data.

Figure 3 is the Nimbus mean cloud values in the Korean area defined by 38.25 to 42.75 degrees north and 123.75 to 128.25 degrees east.

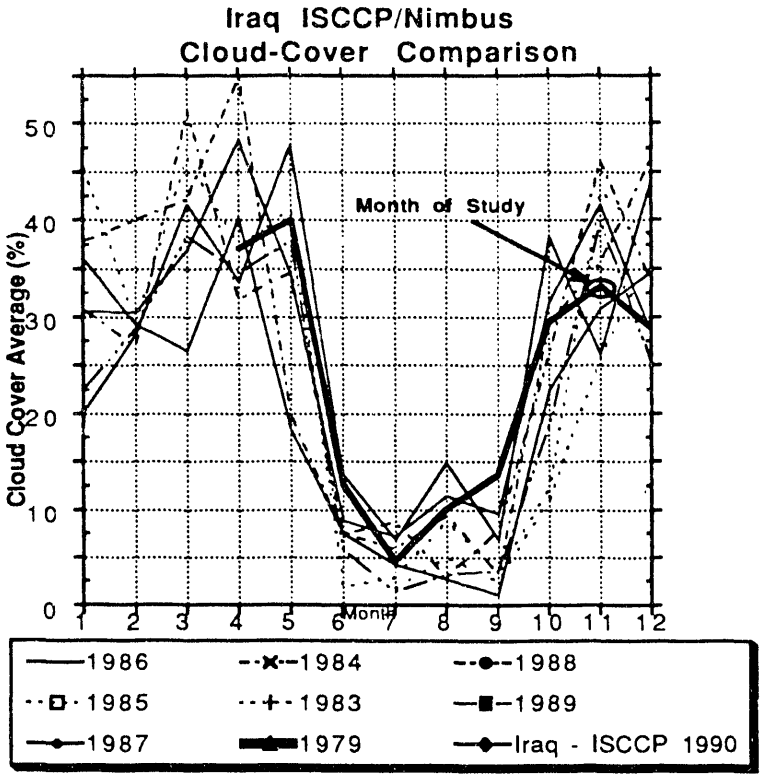


Figure 2. Cloud data from ISCCP database and the Nimbus satellite

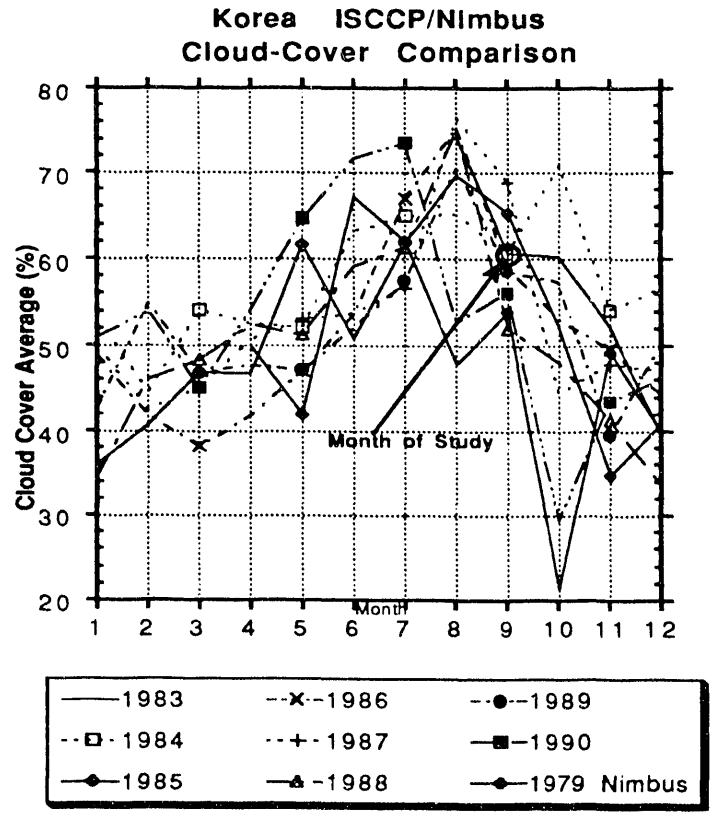


Figure 3. Nimbus mean cloud values in the Korean area defined by 38.25° to 42.75° north and 123.75° to 128.25° east.

The data starts in April 1983. Again one month, September 1984, was selected as a representative cloud-cover month. A full sensitivity analysis using worst and best cloudiness conditions will have to be deferred for the Phase II effort.

### 3.3 Sounding Data

Balloon sounding data was provided by the USAF Environmental Technical Applications Center (USAFETAC) at Scott AFB. Complete upper air information, including individual soundings were provided to determine the height vs. temperature aspect of the study.

### 3.4 Cloud Cover Data Availability

Satellite data over Iraq is difficult to obtain. Figure 4 shows the earth view from various geostationary meteorology satellites. The INSAT satellite, operated by the Indian government, is generally unavailable to either the scientific or military communities on any regular basis. The GOES-1 satellite had fortunately been positioned over the Indian Ocean in 1979, in approximately the same orbit as INSAT, for specific scientific studies. For Phase II, METEOSAT 4 (at 0 degrees East), or the International Cloud Climatology Program (ISCCP) data set will be purchased. ISCCP covers Iraq with polar orbiting TIROS, NIMBUS data as well as METEOSAT geostationary data.

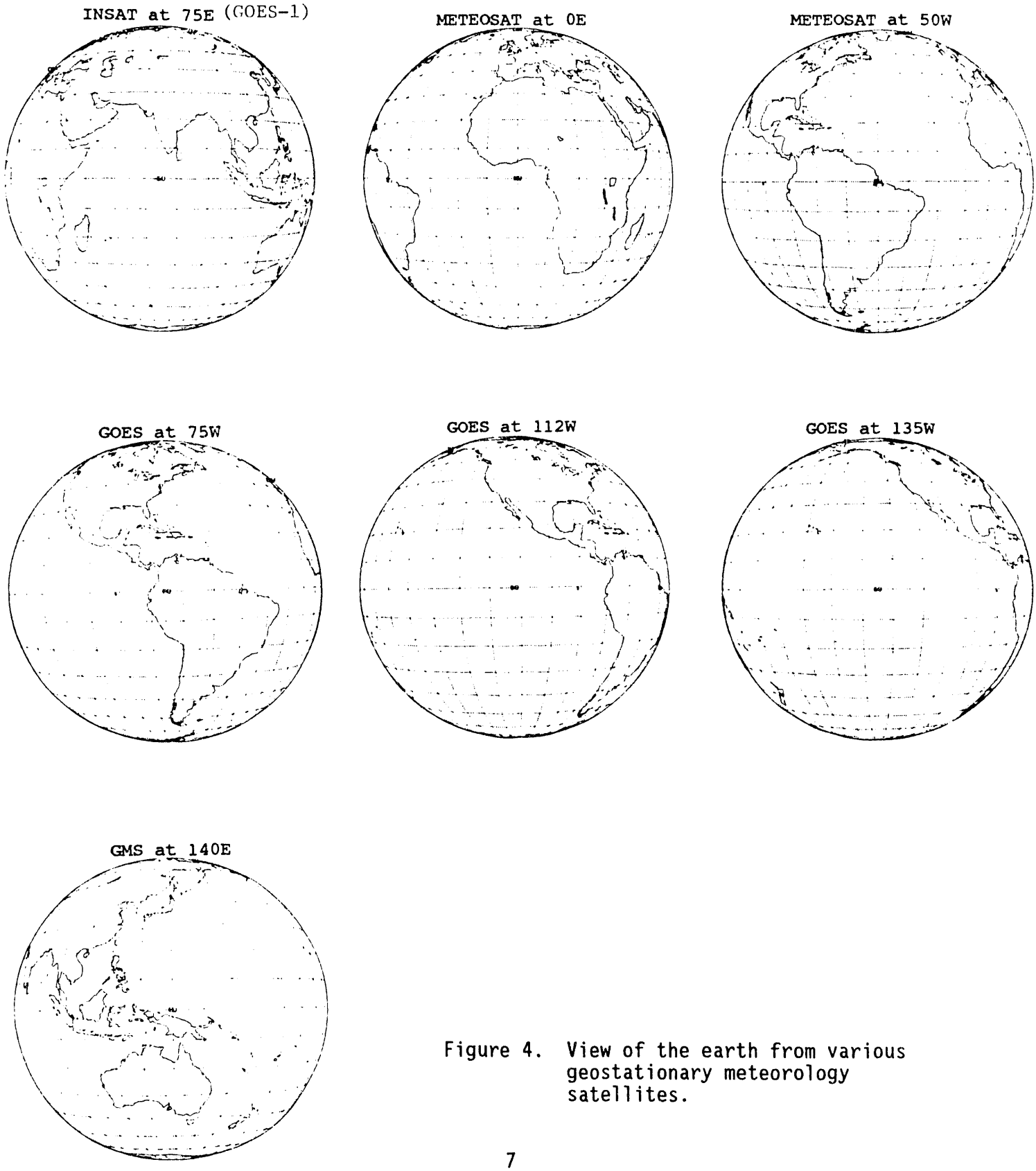


Figure 4. View of the earth from various geostationary meteorology satellites.

## 4.0 TRANSMISSIVITY ANALYSIS

MODTRAN with its LOWTRAN 7.0 module was run for several cases to define transmissivity for clear, and cloudy situations. See F.X. Kneizys et al. (1988) for a detailed description of the LOWTRAN model. Figures 5a and 5b show the geometry of most of the model runs, including cloud-free and cirrus cloud situations. The Korean cases were run with maritime boundary air masses which includes salt aerosols and a high water vapor content. The Iraq cases were run with a desert model that adds dust commensurate with lofted loose dust from a 5 knot wind. The results of the MODTRAN runs are presented in Figures 6-8. Unless indicated, the model runs were in the single scattering mode. Multiple scattering simulations were run but the results were the same as for the single scattering cases.

As per Figure 5, the MODTRAN runs were all run in the slant path mode starting at 60,000 feet or 18.3 km, and run the 0 and 10 km altitude extremes stipulated in the J.B.S. Fax. The range was varied so a representative sampling of transmissivities would be computed. The total transmissivity represents the value computed by the MODTRAN runs and represents the transmissivity through the entire optical path, sensor to target. The normalized transmissivity (1/km) was computed from this value with the following equation:

$$\tau_1 = \exp\left[\frac{1}{\text{Distance(km)}} * \ln(\tau_{\text{total}})\right]$$

where $\tau_1$ is the transmissivity for 1 km and $\tau_{total}$ is the MODTRAN total path transmissivity. This value represents an average transmissivity for the path

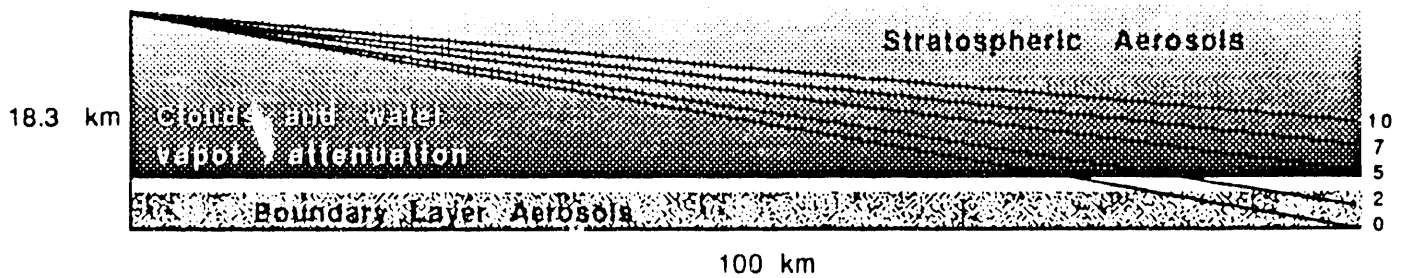


Figure 5. MODTRAN runs in the slant path mode starting at 18.3 km, and run the 0 and 10 km altitude extremes stipulated in the J.B.S. Fax.

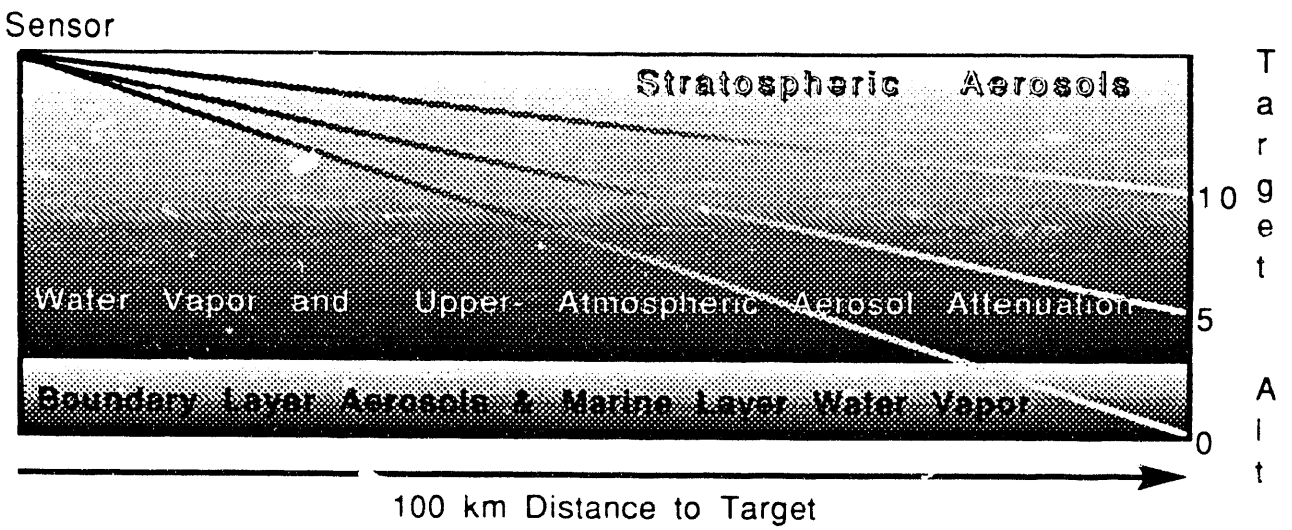


Figure 5a. Modeled Attenuation in Cloud-Free Atmosphere.

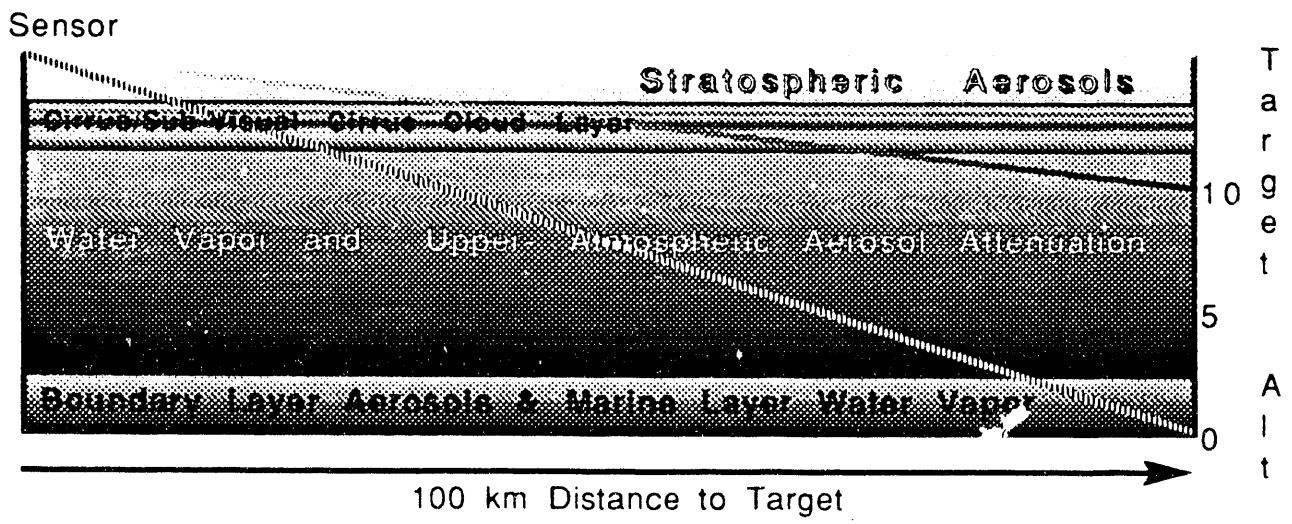


Figure 5b. Modeled Attenuation with Cirrus or Sub-Visible CI Clouds

that includes regions of higher and lower transmissivity due to different modeled concentrations of water vapor and aerosols.

Figure 6 shows the Iraq cases for cloud-free conditions. Transmissivity values are due to molecular scattering, aerosols, and water vapor. Note that the transmissivities for the 4 micron case are higher than the 3 micron cases to the surface but not for the cases that don't penetrate the boundary layer. Summer cases, which contain more water vapor always show lower transmissivities at 3 microns. At 4 microns the seasonal effect is attenuated.

Figure 7 shows the Korean cases of cloud-free conditions. The values and considerations stated for figure 6 still holds. The lower transmissivities for the ground target cases is due to the additional water vapor of the marine air mass used in the simulation.

Figure 8 shows the transmissivities for various cloud types. There was so little difference in transmissivities due to location that only one set is provided (Iraq). The most significant finding from these runs is that water laden cumuliform clouds are effectively opaque to both wavelengths. This will allow phase II computations of sensor probability of seeing to ignore transmissivity effects and to use a binary cloud/cloud-free approach to the sensor to target paths. Generally Figure 8 shows an exponential variation in transmissivity for each of the cloud model runs. The reader may note several features in Figure 8 worth discussion. First, the Winter CI curves in both the 3.0 and 4.0 micron cases show a departure from the exponential curves above the 7 km target altitude. The reason for this is that the model is reflecting the height of the CI cloud. In this case the CI cloud thickness

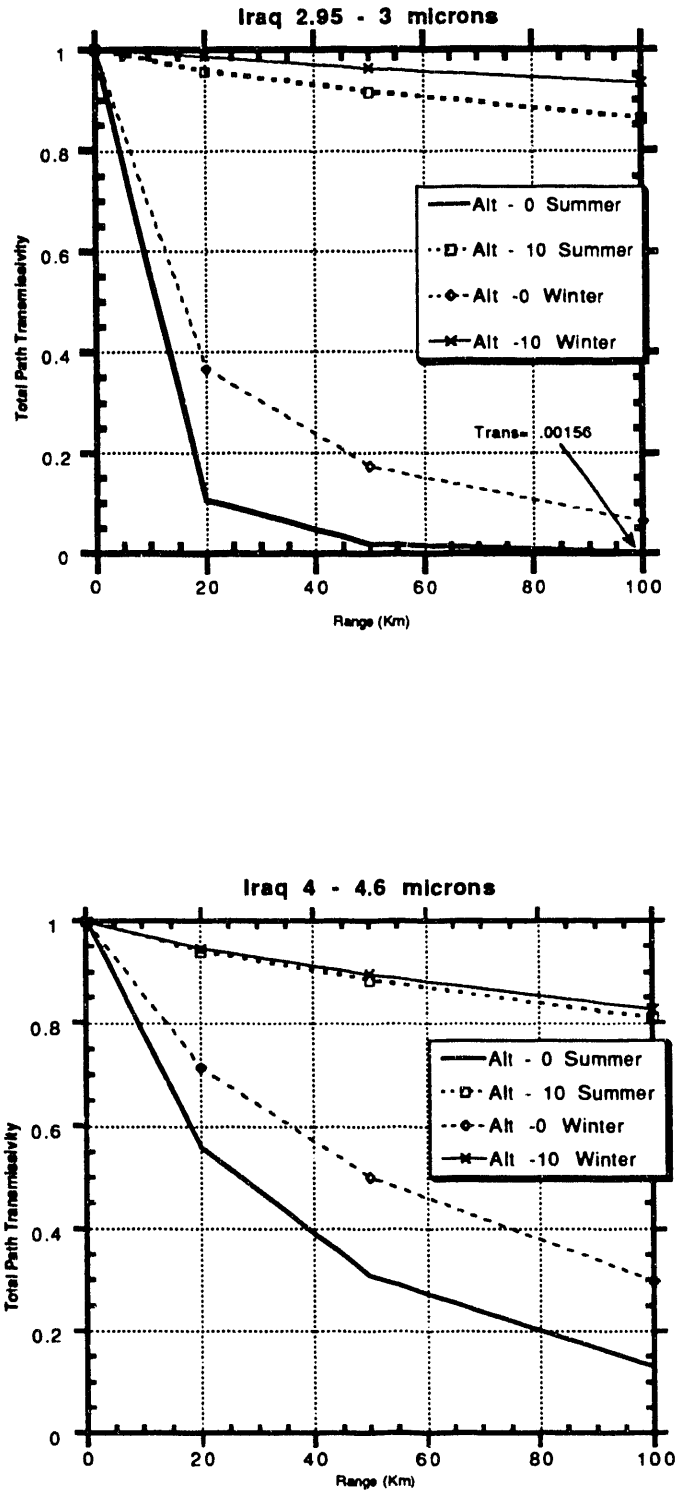


Figure 6. Iraq cases for cloud-free conditions.

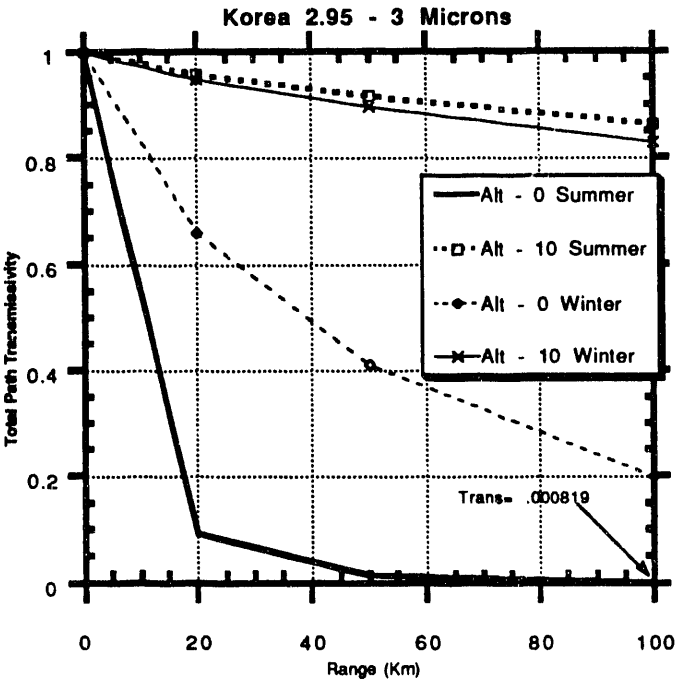


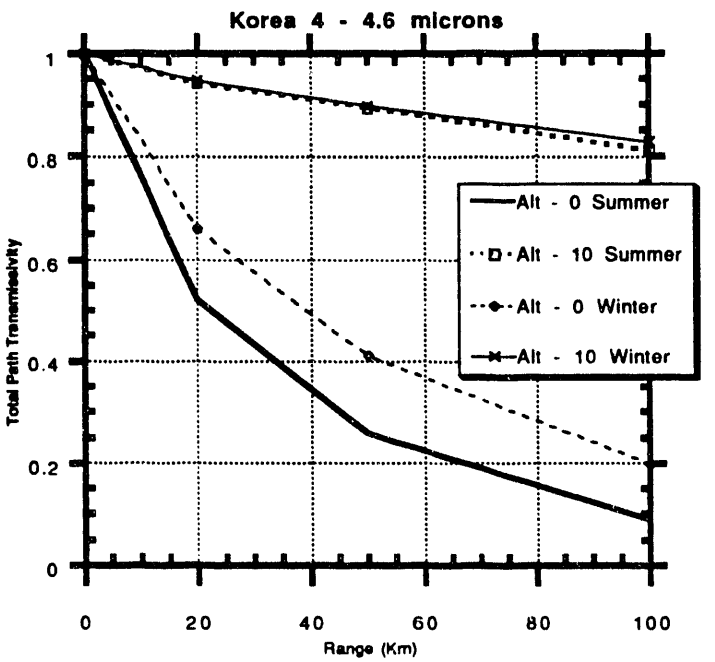


Figure 7. Korean cases of cloud-free conditions.

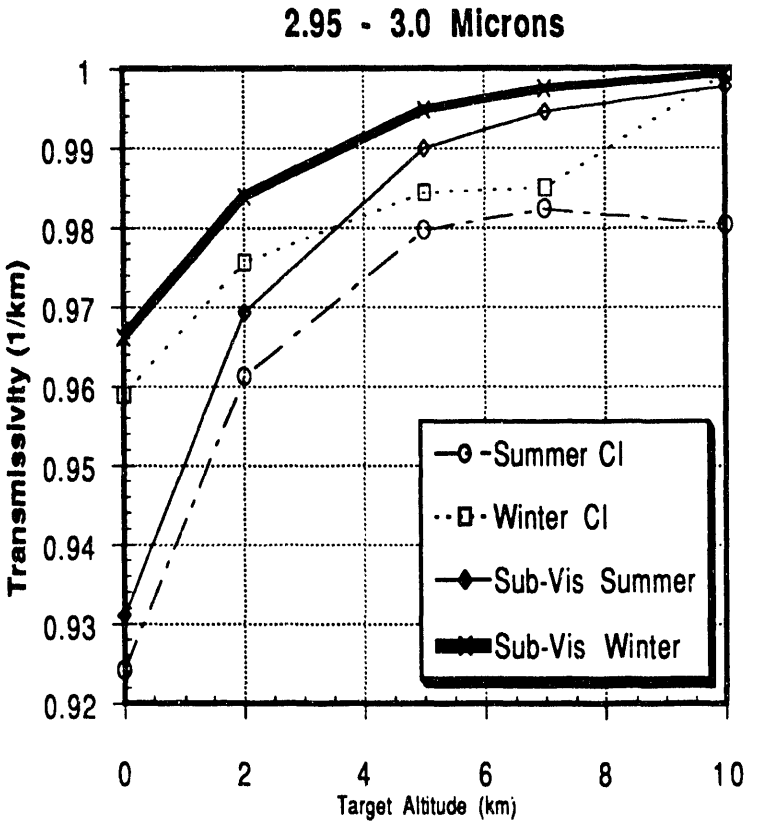


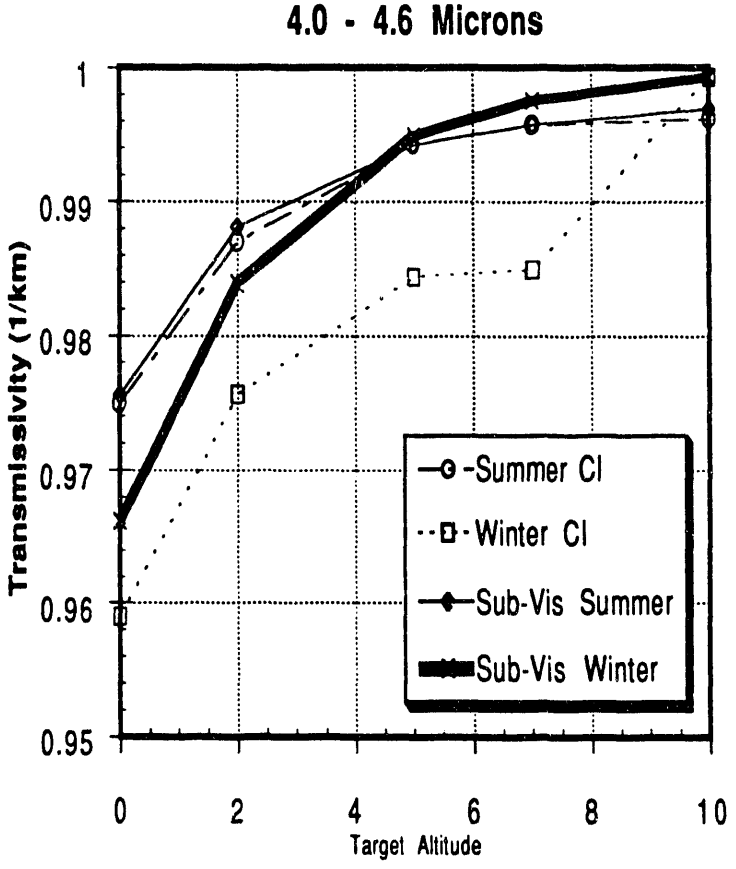


Figure 8. Transmissivities for various cloud types.

includes the 10 km altitude. Viewing geometries from surface to 7 km all represent optical paths through a layer of CI between the sensor at 18.3 km and the target which is below the CI layer. In the 10 km case the target is not below the layer but in it. This increases the optical path fraction in-cloud that results from the straight trigonometric relationship associated with the angle of incidence. (See Figure 9)

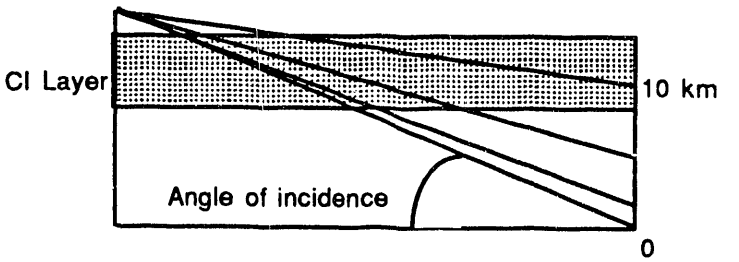


Figure 9. Example of the change in pathlength through a CI layer for different target heights.

The Summer CI 3 micron case reflects another instance where the in-cloud fraction is more than the trigonometric case due to the 18 to 10 km layer being filled with CI cloud. This makes sense since the summer period includes increased CI due to thunderstorms and convection lofting more water vapor into the upper atmosphere. Also note that the SV winter values cross the winter CI values. These crossings are due to the change in modeled thickness of the CI and SV layers, and again where the layer resides in relationship with the target altitude.

### 4.1 Subvisual Cirrus Cloud Transmissivity Considerations

Subvisual cirrus (SV) clouds represent one of the more difficult problems for a transmissivity analysis at high altitudes. A working definition of subvisual cirrus is a cloud that is not observed from the ground or conventional weather satellite, yet is readily observed by a pilot flying at or near the same altitude as the cloud. Subvisual cirrus's transmissivity

at visual and IR wavelengths is too high to be detected by vertically pointing imaging systems. Aircraft detect this cloud type because they are seeing the cloud edge-on. Ground-based lidar systems can detect SV but lidar systems are not deployed in synoptic networks. SV can be detected, and have been the subject of scientific investigation, but are not detected in any systematic way. As a result, there is no climatology of SV available from the operational meteorological community.

Fortunately, The Stratospheric Aerosol and Gas Experiment (SAGE) satellite program sampled the atmosphere tangentially and collected CI and SV data in the 1980s, (Woodbury and McCormick 1986). This paper presents statistics for a 34 month period (February 1979 to November 1981), including what they term optically thin cirrus clouds - or SV. Although not explicitly combined with the GOES-1 and GMS data for phase I, this climatology can be combined with the other conventional cloud statistics as a Phase II effort. Figure 10 shows the cloud distribution statistics for SV by latitude band. Figures 11, 12, 13 and 14 show the same distributions by season.

Additionally, a review of the literature (Sassen and Cho 1992) indicates that the lower limits of transmissivity for SV is around .97 per km. Our own calculations, based on a Mie scattering simulation, indicates a transmissivity of .98 and an average thickness of the cloud as 0.6 km. Assuming the height of the cloud is anywhere from 5.92 km (20,000 ft) to 13.32 km (45,000), then the range of transmissivities for the Raptor geometries is shown in Figure 15. Figure 15 shows the transmissivity degradation due strictly to SV while Figure 8 show the transmissivity degradation due to SV and a cloud free atmosphere. Notice that Figure 8

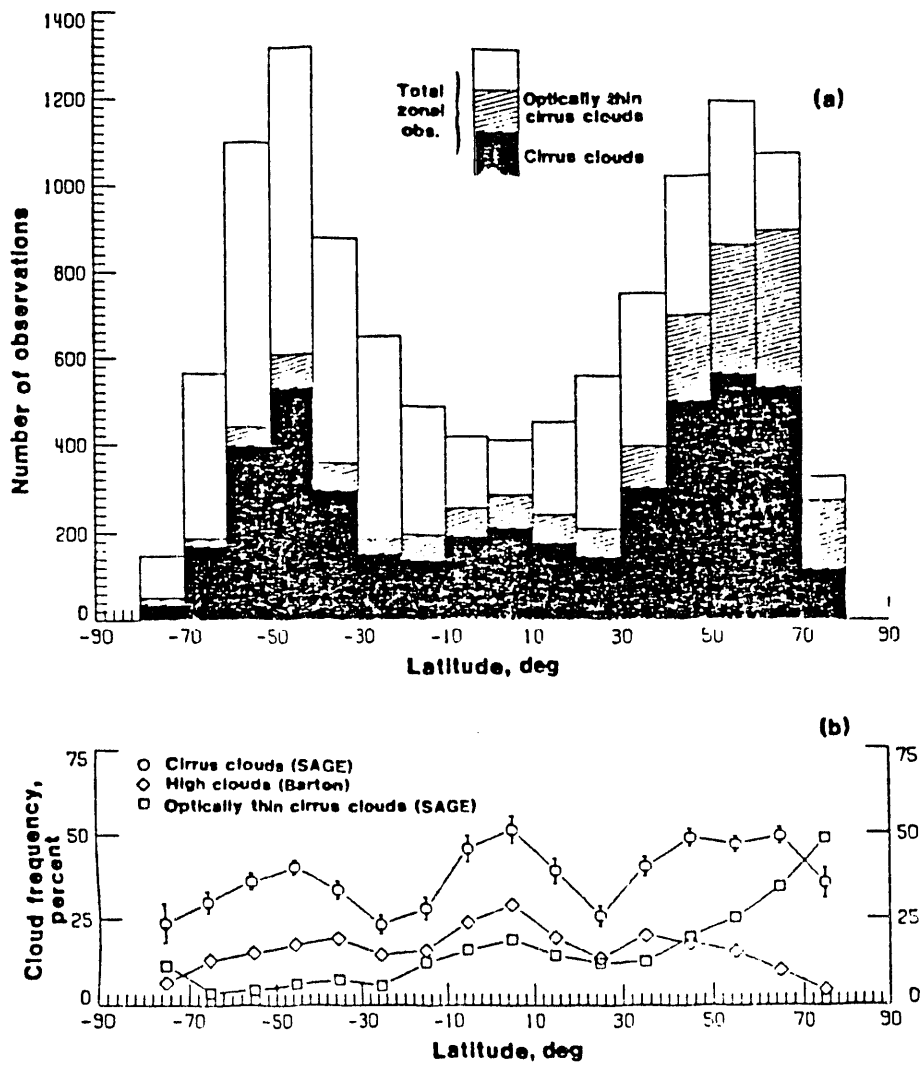


Figure 10. Cloud distribution statistics for SV by latitude band.

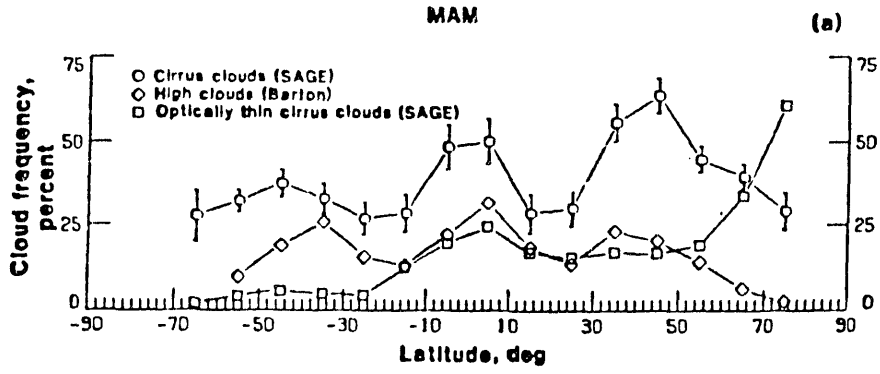


Figure 11.



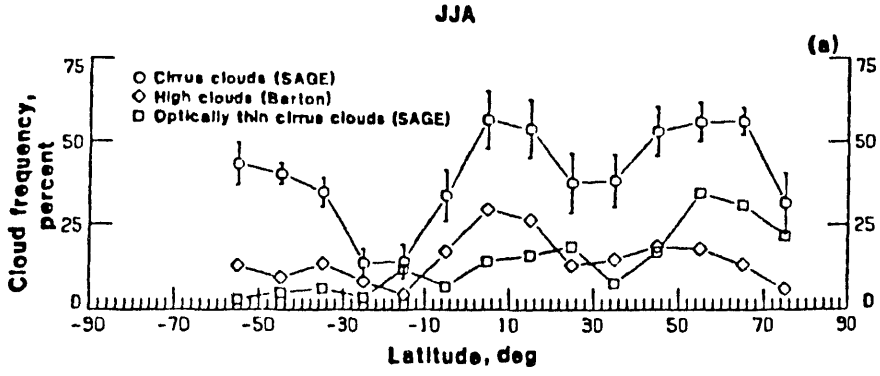


Figure 12.



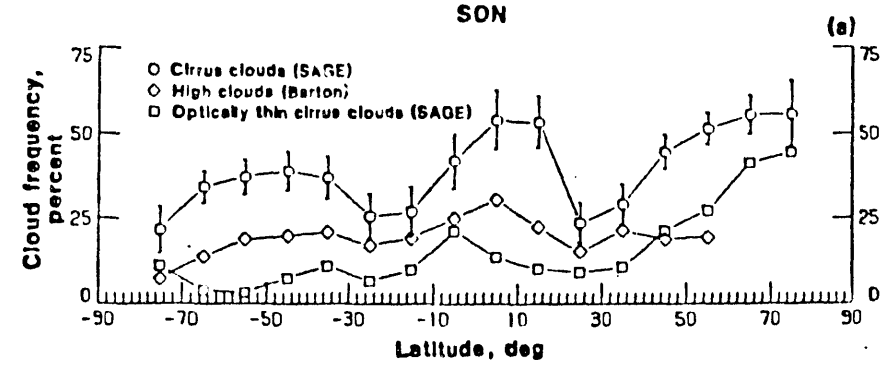


Figure 13.



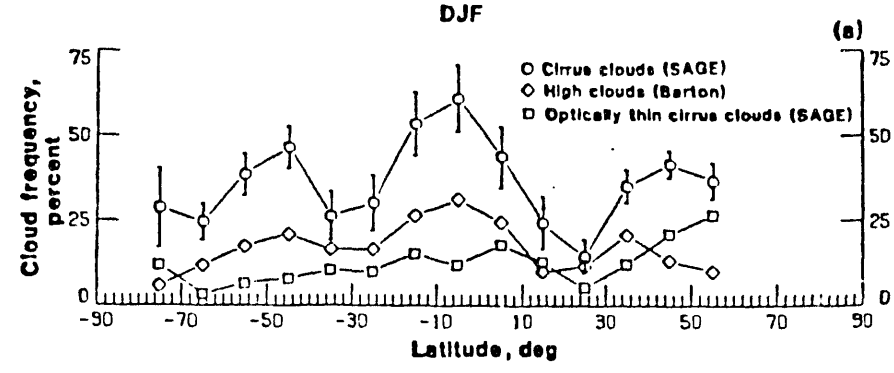


Figure 14.

Figures 11, 12, 13, and 14. Cloud distribution statistics for SV by season.

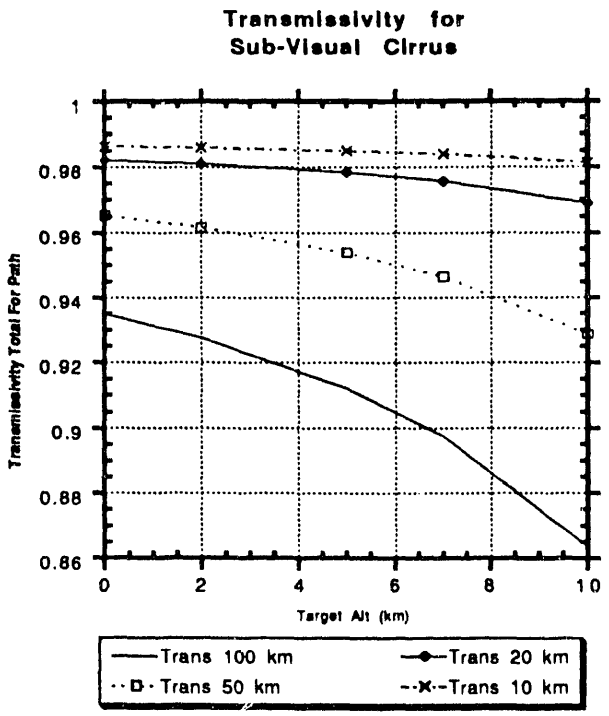


Figure 15. Range of transmissivities for the Raptor geometries.

shows a frequency dependence due to the clear atmosphere's contribution to transmissivity in the lower atmosphere, not due to the SV whose attenuation isfrequency independent in the IR region of concern. Figure 15 holds the SV thickness constant at 0.6 km whereas MODTRAN varies the cloud thickness with the season. The calculations for Figure 15 assume the SV is always below 18.3 km, the altitude of the sensor.

## 5.0 CLOUD ANALYSIS

Each figure shows the cloud free line of site (CFLOS) probability, averaged over all azimuths for specific locations in Iraq and Korea. Each figure breaks out the CFLOS probabilities for the altitudes (0, 2, 5, 7, and 10 km) that were specified by the sponsor. Two Universal times: 0000 UTC about 10 PM local), and 1200 UTC (about 10 AM local) were analyzed for Iraq. 0600 UTC (about 3 PM local) was analyzed for Korea. The first slant path distance value is at 18 km, the specified altitude of the sensor.

The analysis locations for Iraq and North Korea were selected for their climatology.

| | Site | Lat | Long |
|---|---|---|---|
| North Korea | 1 | 39.8° | 126.5° |
| Iraq | 1 | 32.8° | 40.1° |
| | 2 | 32.8° | 44.0° |
| | 3 | 31.0° | 47.0° |

The North Korea locations is about 100 km west of the East Korea Bay coast line about 200 km north of the South Korean border. This site is in the Taedong River valley with highlands to the east and a broad coastal plane to the west.

Iraqi site 1 is in western Iraq in the Syria Desert.

Iraqi site 2 is near Karbala just east of the Razaza Reservoir.

Iraqi site 3 is near the Tigris River Marshes and also near the Iran Border.

## 5.1 Iraq

Figures 16-22 display the results of the cloud-freeness interrogations of the satellite cloud data discussed earlier.

### 5.1.1 Discussion

As expected, the analysis showed very little variation with distance because the data was averaged over all azimuths. The following figure shows how the probability for a CFLOS is affected by a single cloud.

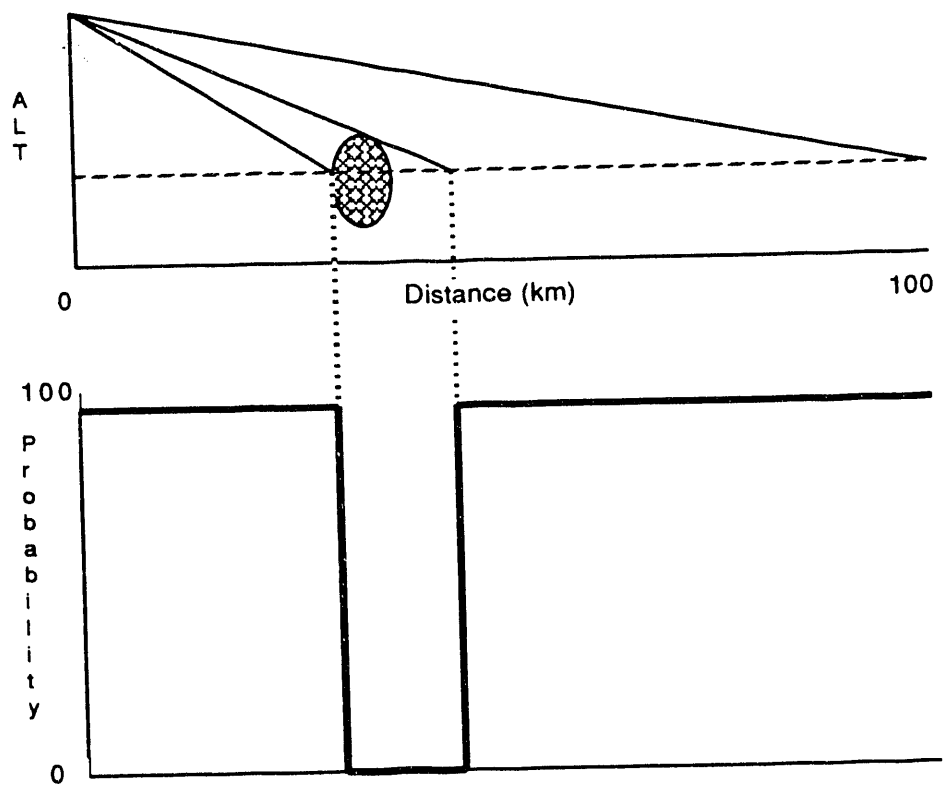


If this case is run for all azimuths where clouds are fairly randomly distributed, the zero probability delta in the probability plot smears over all distances. The only case where this weak relationship strengthens is in a case where there is a very persistent cloud structure (one anchored to a geographical feature of many days). An example of this kind of feature is

seen in Figure 21. In this figure a persistent cloud feature occurs about 25-30 km from site location 3 at 1200 UTC. Another consistent result illustrated in the figures is a strong dependence on target altitude. In all cases, the 10 km probability of CFLOS is higher than for a lower altitude target. The zero altitude target cases averaged together (Figure 22) show about a 72 percent clear line of sight value (28 percent cloudy) which matched reasonably well with Figure 2's value of 33 percent for the entire Iraq area.

**Site 1 0000 UTC analysis** - Figure 16 shows an almost totally clear situation for the 10 km case and some close-in cloud effects at 7 and 5 km target altitudes which results in a monotonically decreasing probability at the lower altitudes. This can be easily simulated with a relatively thin middle cloud deck persisting at the 5-7 km altitude level.

**Site 1 1200 UTC analysis** - Figure 17 shows a persistent "clear" hole in the 25-45 km distance for the 10 km target case.

**Site 2 0000 UTC analysis** - Figure 18 shows totally clear conditions at 10 km and fairly random distributions of clouds affecting the 5 and 7 km target scenarios. A relatively speaking "clear hole" is present for the low level target scenarios from 45-75 km distances.

**Site 2 1200 UTC analysis** - Figure 19 shows no unexpected features.

**Site 3 0000 UTC analysis** - Figure 20 shows the strongest probability with distance behavior of any of the cases. This would be easily explained by an evenly distributed, scattered cloud deck below 5 km altitude.

**Site 3 1200 UTC analysis** - Figure 21 shows the artifact of a very persistent cloud feature that reaches periodically to 5 km but is very evident at 2 km and below starting at about 25 km. Beyond 45 km the CFLOS values recover indicating that there is less cloud at distances beyond 50 km.

Comparing the 0 and 12 UTC probabilities for the sites, Sites 1 and 3 show 10% more cloudiness in the afternoon (12 UTC) vs. morning (0 UTC) composites. Site 2 does not show this large diurnal tendency. Sites 1 and 3 are typical of many areas that show cloud development during the day due to surface heating. Site 2, near Baghdad, is in a wet region where afternoon cloud buildups are suppressed

Figure 22 is an average of all Iraq data (all sites and both times). Note that the monotonically decreasing values at the lower target altitudes is exactly the behavior you would expect from a low resolution cloud data base study.

Tables 1 and 2 show the cloud maximum and minimum height (in meters) log file for each of the all-azimuth runs analyzed. Table 1 shows the maximum cloud tops determined each time for the three Iraqi sites. Table 2 shows the cloud bases as determined from the Baghdad sounding.

Figure 23 shows a subset of the 1200 UTC Site 3 data. Here a specific azimuth (75 degrees east of north) is accumulated to show how the persistent cloud structures standout when the statistics are not accumulated by averaging all azimuth angles.

### 5.2 Korea

Due to the limited time and budget we were only able to make one Korean run. We choose 0600 UTC. Figure 24 shows the same information as in the Iraq cases. The all-azimuth runs show similar behavior as seen in the Iraq runs. The only difference is the lower CFLOS probability values due to the expected higher cloud cover in North Korea.

Figures 25 and 26 show CFLOS probabilities for a west and east looking azimuth for the same situation as Figure 25. In the east view azimuth the ridge line 70-80 km away does show up in the cloud statistics.

Tables 3 and 4 show the cloud maximum and minimum height (meters) log file for the Korean run. Note the 16243 meter thunderstorm top.

## 6.0 CONCLUSIONS

From a meteorological perspective Raptor will not be overwhelmed by cloud cover in either Iraq or Korea. Above 7 km targets will have a CFLOS probability of over 85 percent. As Figures 23, 25 and 26 illustrate, the cloud cover at specific azimuthal bearings does drop to lower values but a constellation of Raptor sensors should help overcome this problem.

Clear air transmissivities were better than 8 percent at 4.0 microns for all seasons and locations. At 3 microns, the worst case transmissivity drops to .08 percent.

Even pervasive sub-visual cirrus clouds would only reduce the transmissivity of the clear air cases at 10 km distances by 13 percent.

## 7.0 PHASE II RECOMMENDATIONS

- Establish the CFLOS probability for a constellation of Raptor sensors. Since the CFLOS is highly variable with azimuth, and cloud patterns are to some degree anchored to terrain, a multi-sensor CFLOS value is likely to be much better than for any given single sensor.

- Since CFLOS varies with season, time of day, distance, altitude of target, and azimuth no two dimensional graph can provide all available information. As a result, Phase II should develop a database and extraction routine to allow the CFLOS (and transmissivities) to be extracted for use in probability of detection simulations.

- Raptor's detection and engagement probability is also to some degree sensitive to the temporal and spatial variation in clouds over a few kilometers and one or two hours. Therefore, a detailed analysis of CFLOS's variance with respect to time and location of the sensor should be completed.

- Budget permitting, Phase II should also expand the statistical robustness of the analysis to include multi-year, and multi-time-of-day data analysis.

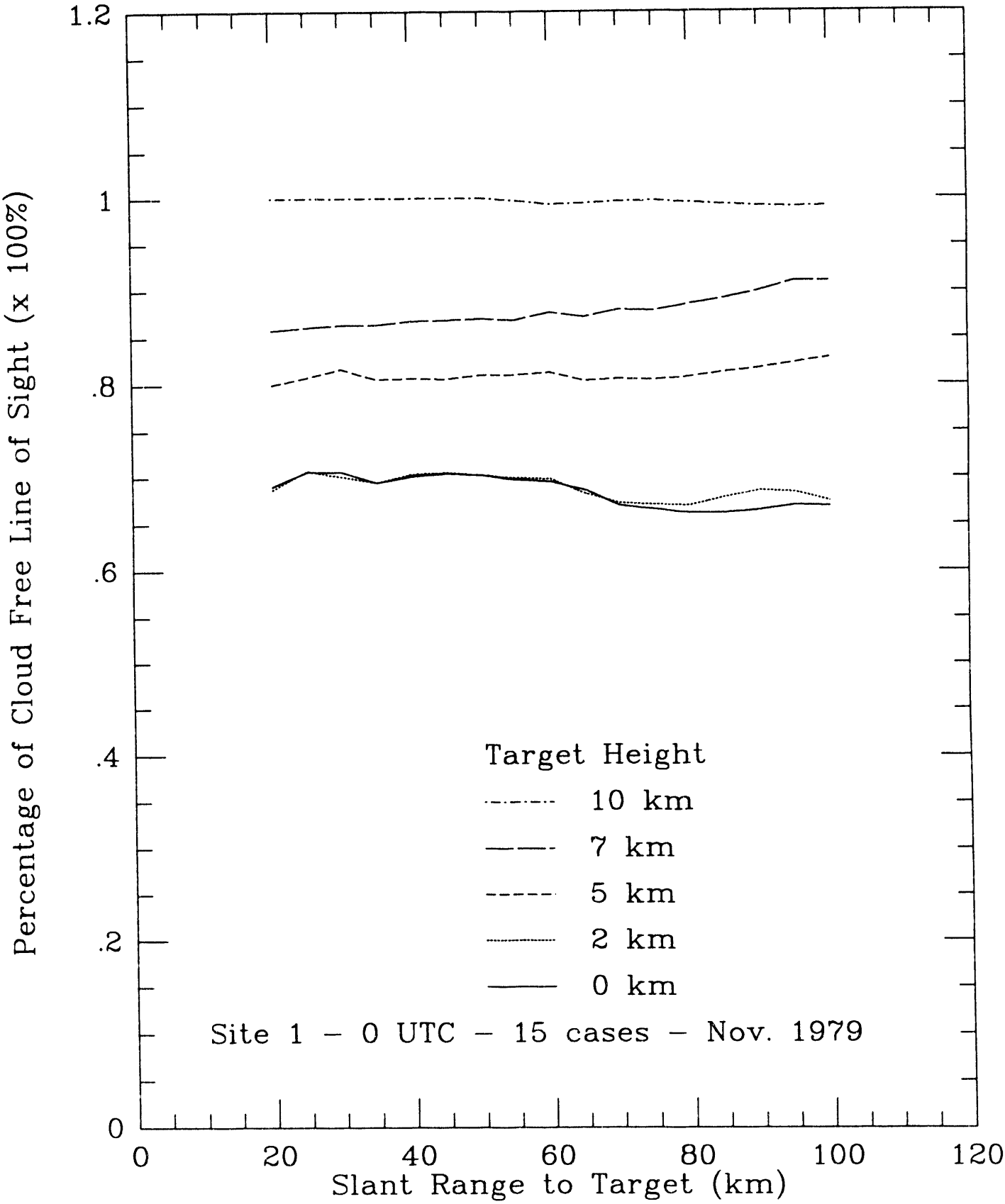
1.2
1
.8
.6
.4
.2
0
Percentage of Cloud Free Line of Sight (x 100%)
0
20
40
60
80
100
120
Slant Range to Target (km)
Target Height
10 km
7 km
5 km
2 km
0 km
Site 1 - 0 UTC - 15 cases - Nov. 1979

Figure 16.

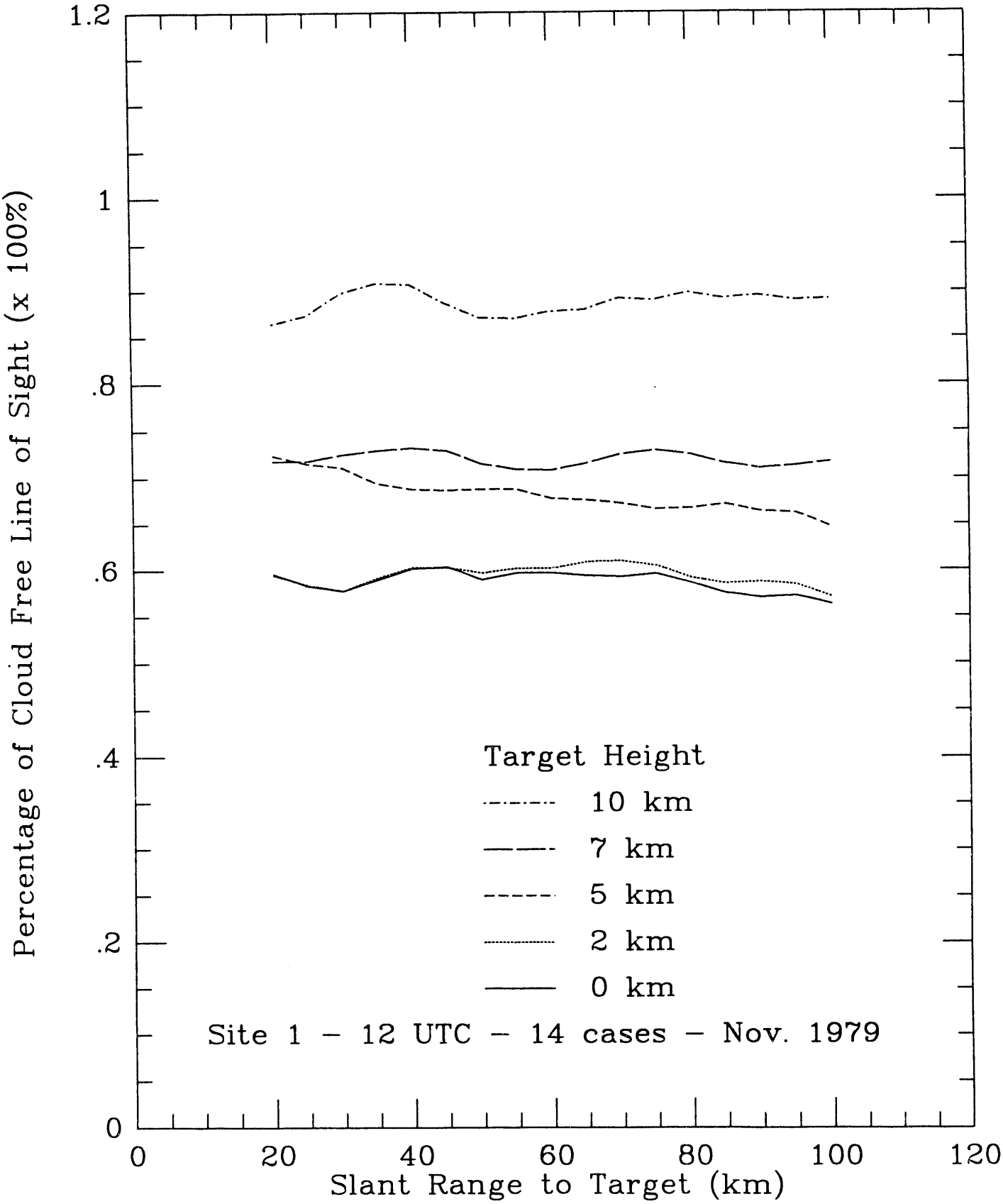
1.2
1
.8
.6
.4
.2
0
Percentage of Cloud Free Line of Sight (x 100%)
Target Height
10 km
7 km
5 km
2 km
0 km
Site 1 – 12 UTC – 14 cases – Nov. 1979
0
20
40
60
80
100
120
Slant Range to Target (km)

Figure 17.

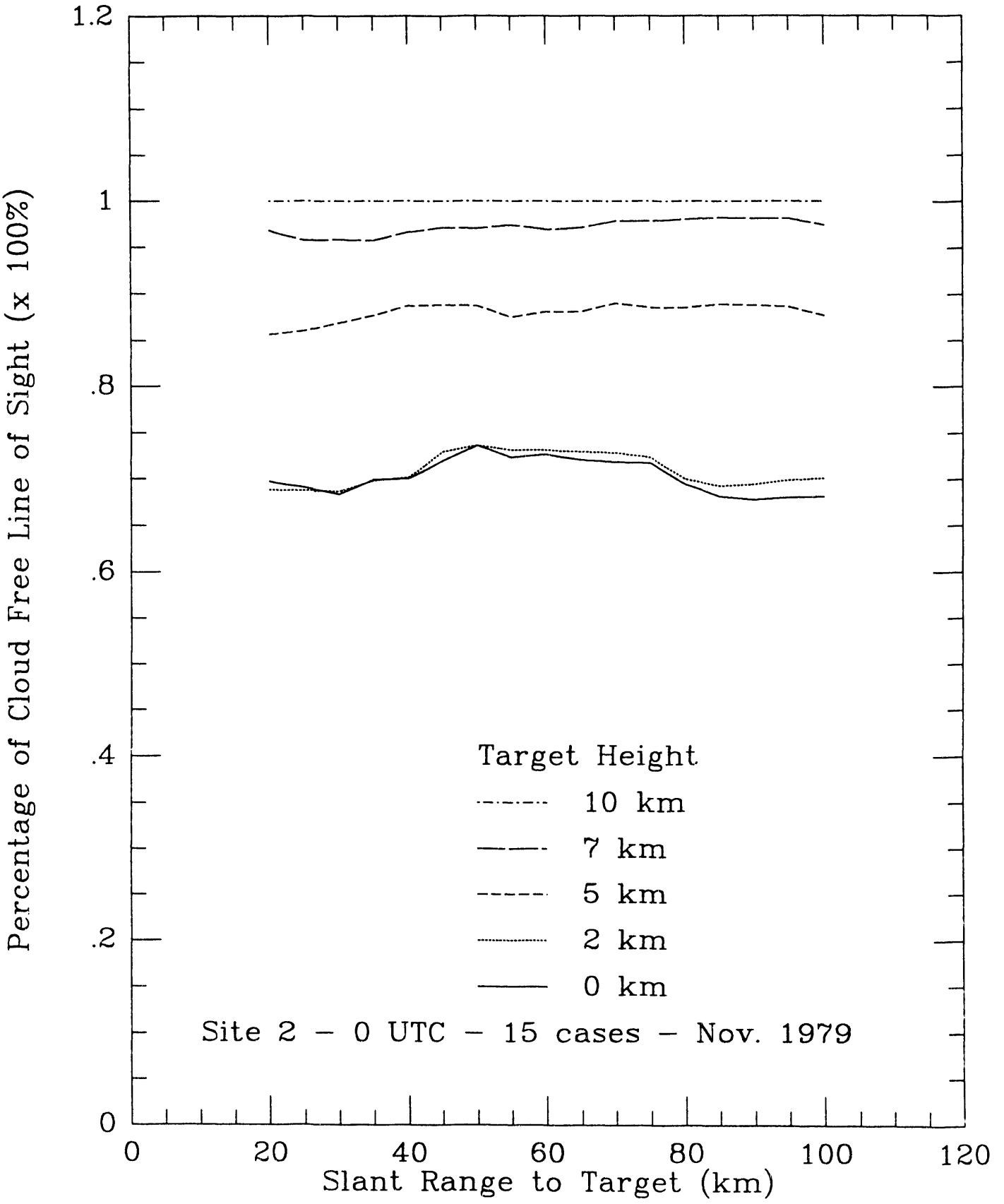
1.2
1
.8
.6
.4
.2
0
Percentage of Cloud Free Line of Sight (x 100%)
Target Height
10 km
7 km
5 km
2 km
0 km
Site 2 – 0 UTC – 15 cases – Nov. 1979
0
20
40
60
80
100
120
Slant Range to Target (km)

Figure 18.

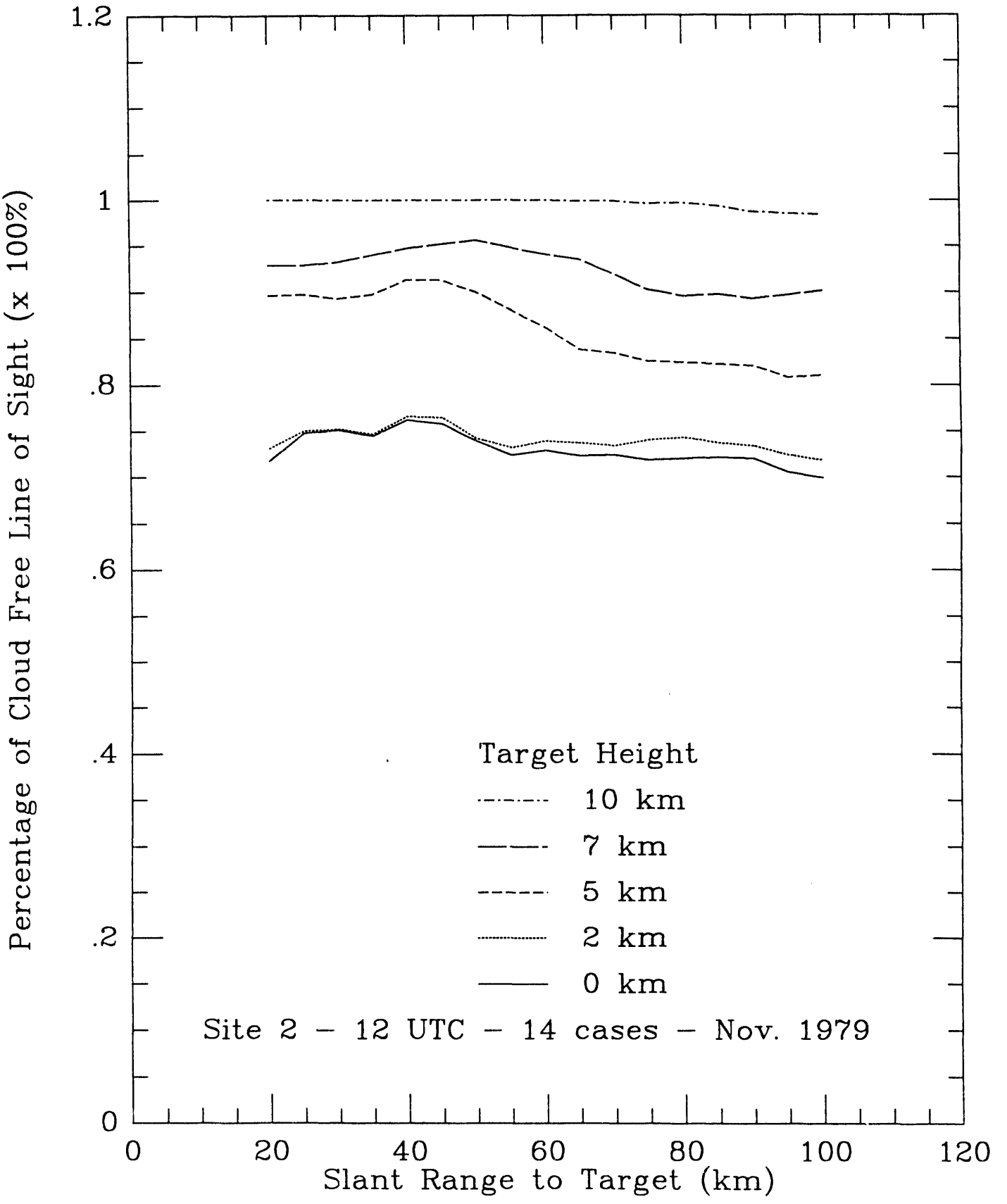
1.2
1
.8
.6
.4
.2
0
Percentage of Cloud Free Line of Sight (x 100%)
0
20
40
60
80
100
120
Slant Range to Target (km)
Target Height
10 km
7 km
5 km
2 km
0 km
Site 2 - 12 UTC - 14 cases - Nov. 1979

Figure 19.

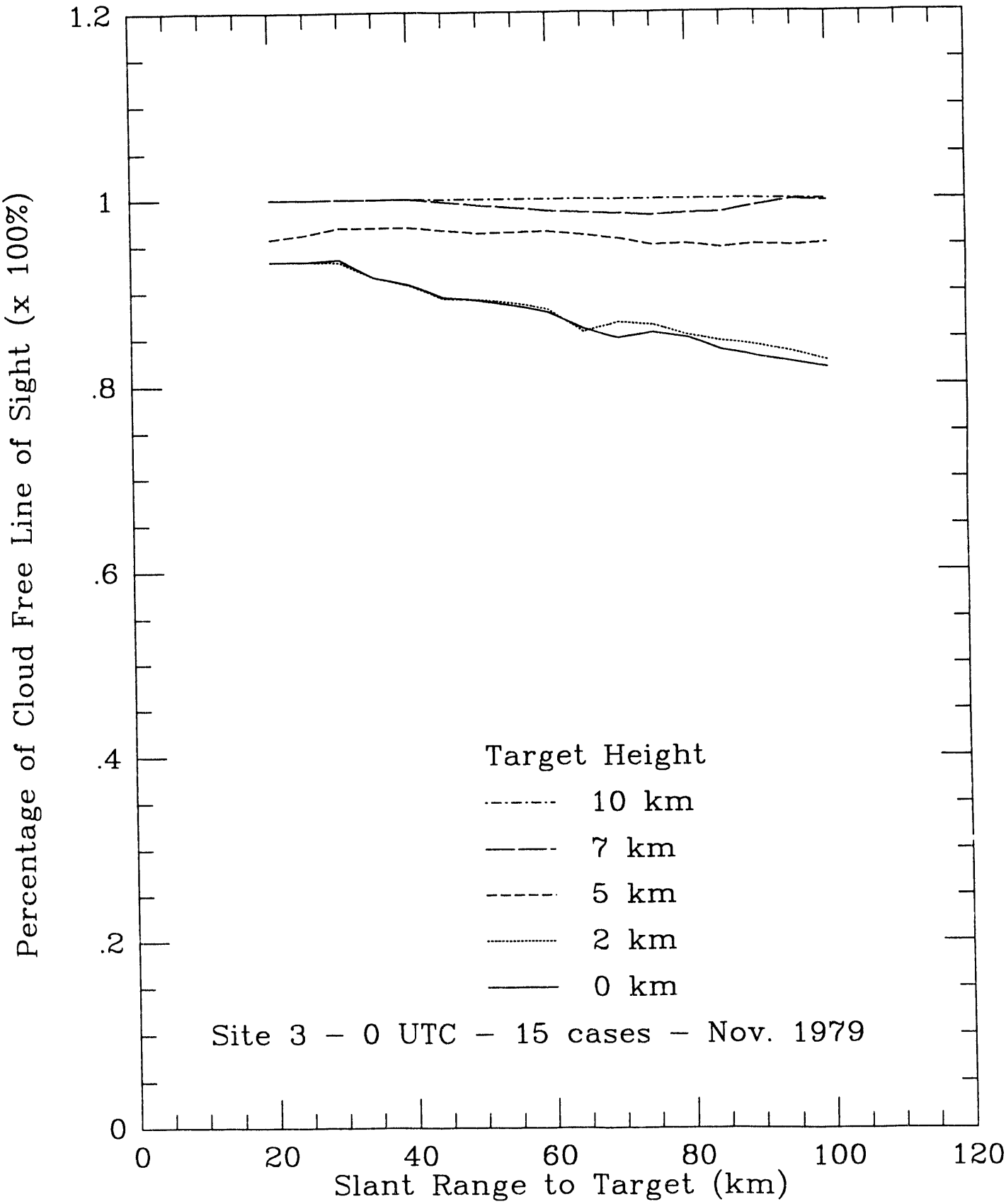
1.2
1
.8
.6
.4
.2
0
Percentage of Cloud Free Line of Sight (x 100%)
0
20
40
60
80
100
120
Slant Range to Target (km)
Target Height
10 km
7 km
5 km
2 km
0 km
Site 3 – 0 UTC – 15 cases – Nov. 1979

Figure 20.

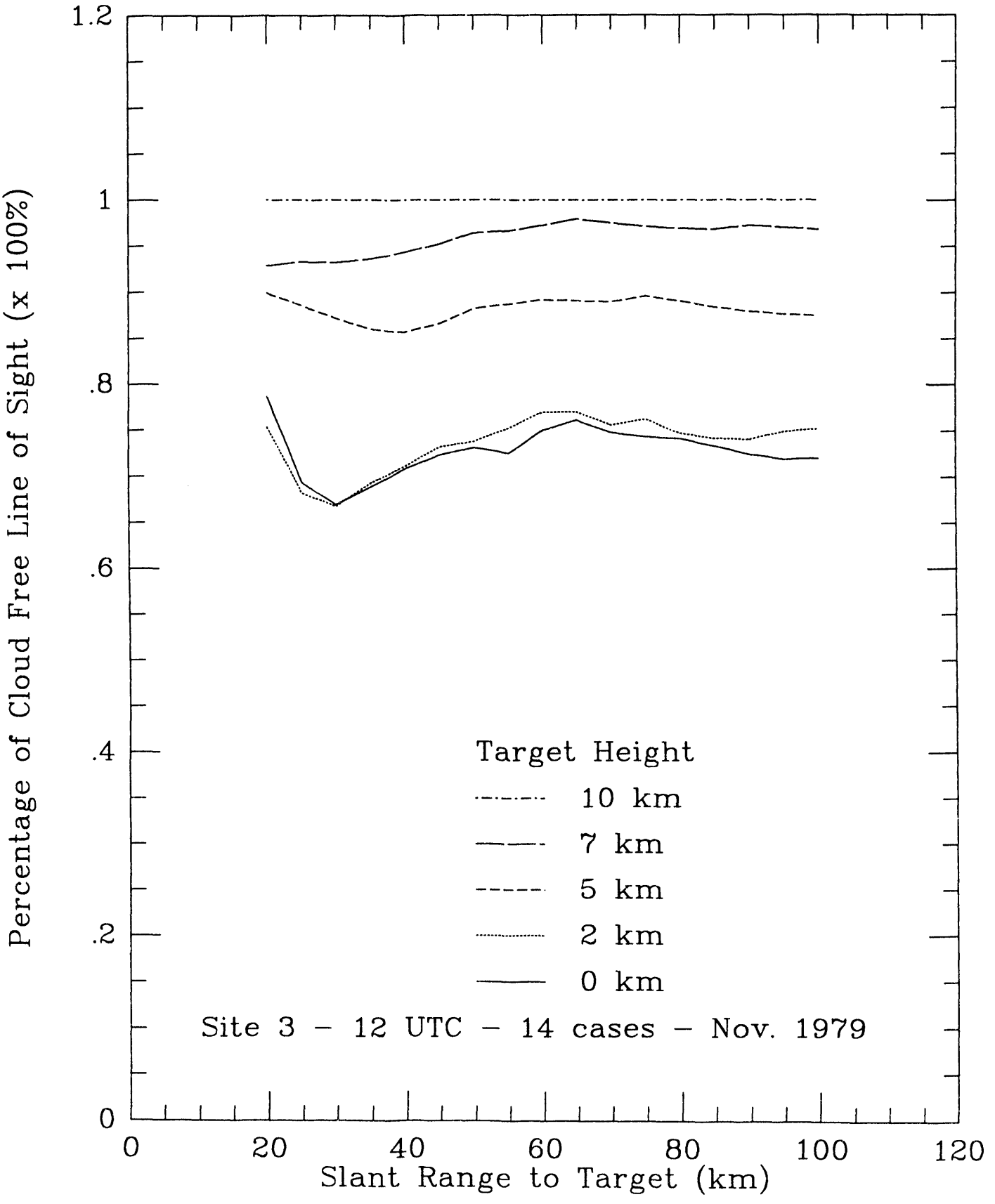
1.2
1
.8
.6
.4
.2
0
Percentage of Cloud Free Line of Sight (x 100%)
Target Height
10 km
7 km
5 km
2 km
0 km
Site 3 - 12 UTC - 14 cases - Nov. 1979
0
20
40
60
80
100
120
Slant Range to Target (km)

Figure 21.

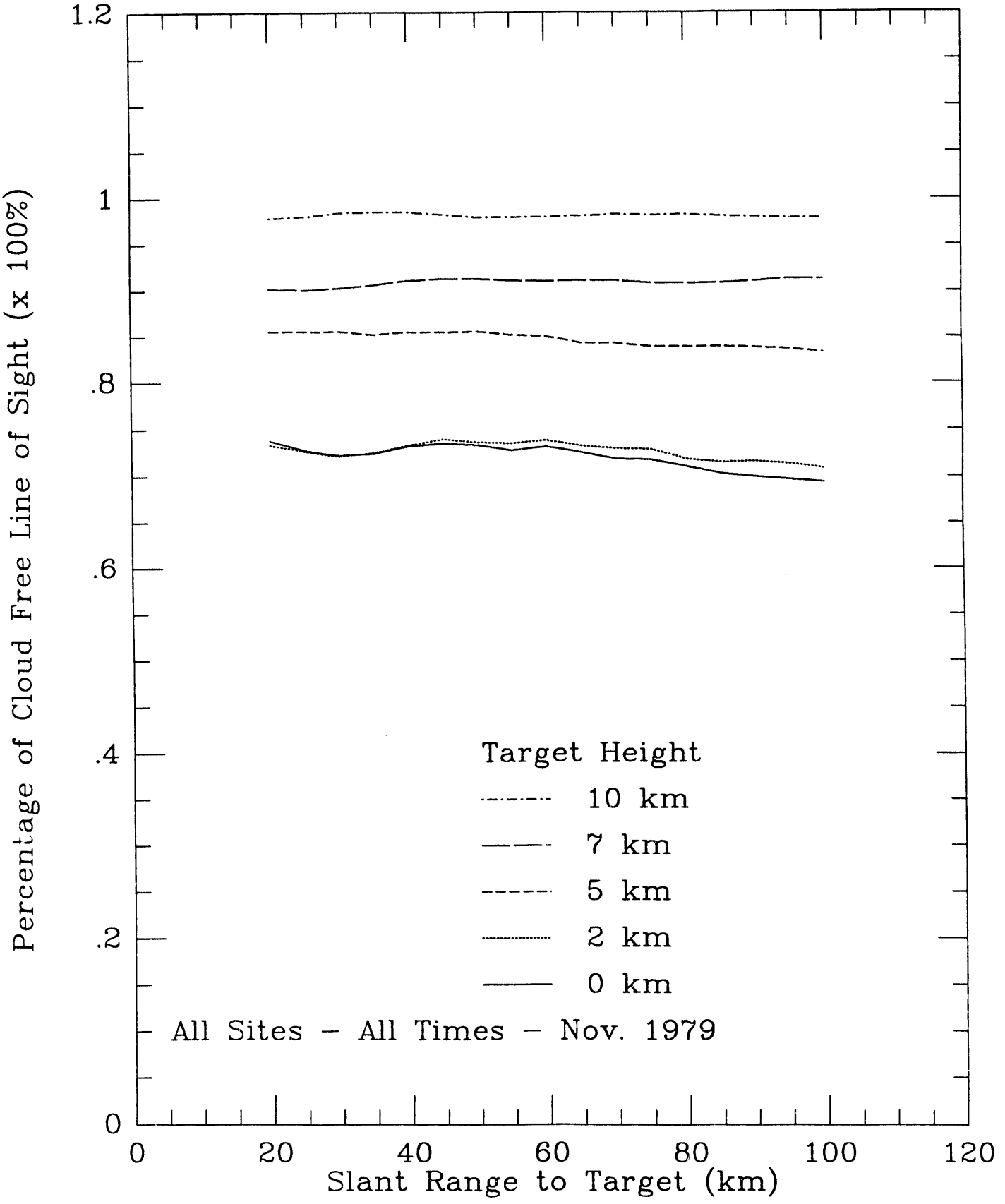
Percentage of Cloud Free Line of Sight (x 100%)
1.2
1
.8
.6
.4
.2
0
0
20
40
60
80
100
120
Slant Range to Target (km)
Target Height
10 km
7 km
5 km
2 km
0 km
All Sites – All Times – Nov. 1979

Figure 22.

| | |
|---|---|
| Max cloud top (m) | 0 |
| Max cloud top (m) | 8047 |
| Max cloud top (m) | 6879 |
| Max cloud top (m) | 7066 |
| Max cloud top (m) | 0 |
| Max cloud top (m) | 7100 |
| Max cloud top (m) | 7100 |
| Max cloud top (m) | 10939 |
| Max cloud top (m) | 11380 |
| Max cloud top (m) | 0 |
| Max cloud top (m) | 0 |
| Max cloud top (m) | 3253 |
| Max cloud top (m) | 4661 |
| Max cloud top (m) | 0 |
| Max cloud top (m) | 5437 |
| Max cloud top (m) | 5305 |
| Max cloud top (m) | 9892 |
| Max cloud top (m) | 10048 |
| Max cloud top (m) | 7243 |
| Max cloud top (m) | 4780 |
| Max cloud top (m) | 5060 |
| Max cloud top (m) | 4145 |
| Max cloud top (m) | 5599 |
| Max cloud top (m) | 7030 |
| Max cloud top (m) | 9591 |
| Max cloud top (m) | 4231 |
| Max cloud top (m) | 7323 |
| Max cloud top (m) | 6096 |
| Max cloud top (m) | 5494 |
| Max cloud top (m) | 7453 |
| Max cloud top (m) | 4178 |
| Max cloud top (m) | 9399 |
| Max cloud top (m) | 5659 |
| Max cloud top (m) | 8456 |
| Max cloud top (m) | 7134 |
| Max cloud top (m) | 0 |
| Max cloud top (m) | 4423 |
| Max cloud top (m) | 8387 |
| Max cloud top (m) | 0 |
| Max cloud top (m) | 10584 |
| Max cloud top (m) | 7724 |
| Max cloud top (m) | 0 |
| Max cloud top (m) | 10527 |
| Max cloud top (m) | 10527 |
| Max cloud top (m) | 9134 |
| Max cloud top (m) | 4631 |
| Max cloud top (m) | 8464 |
| Max cloud top (m) | 8956 |
| Max cloud top (m) | 0 |
| Max cloud top (m) | 0 |
| Max cloud top (m) | 0 |
| Max cloud top (m) | 0 |
| Max cloud top (m) | 0 |
| Max cloud top (m) | 0 |
| Max cloud top (m) | 2936 |
| Max cloud top (m) | 3048 |
| Max cloud top (m) | 0 |
| Max cloud top (m) | 0 |
| Max cloud top (m) | 0 |
| Max cloud top (m) | 0 |
| Max cloud top (m) | 0 |
| Max cloud top (m) | 0 |
| Max cloud top (m) | 5254 |
| Max cloud top (m) | 4533 |
| Max cloud top (m) | 4865 |
| Max cloud top (m) | 4533 |
| Max cloud top (m) | 13561 |
| Max cloud top (m) | 5063 |
| Max cloud top (m) | 4732 |
| Max cloud top (m) | 9465 |
| Max cloud top (m) | 5465 |
| Max cloud top (m) | 4973 |
| Max cloud top (m) | 4850 |
| Max cloud top (m) | 0 |
| Max cloud top (m) | 0 |
| Max cloud top (m) | 0 |
| Max cloud top (m) | 0 |
| Max cloud top (m) | 0 |
| Max cloud top (m) | 12818 |
| Max cloud top (m) | 6081 |
| Max cloud top (m) | 4881 |
| Max cloud top (m) | 5794 |
| Max cloud top (m) | 9536 |
| Max cloud top (m) | 5192 |

Table 1.

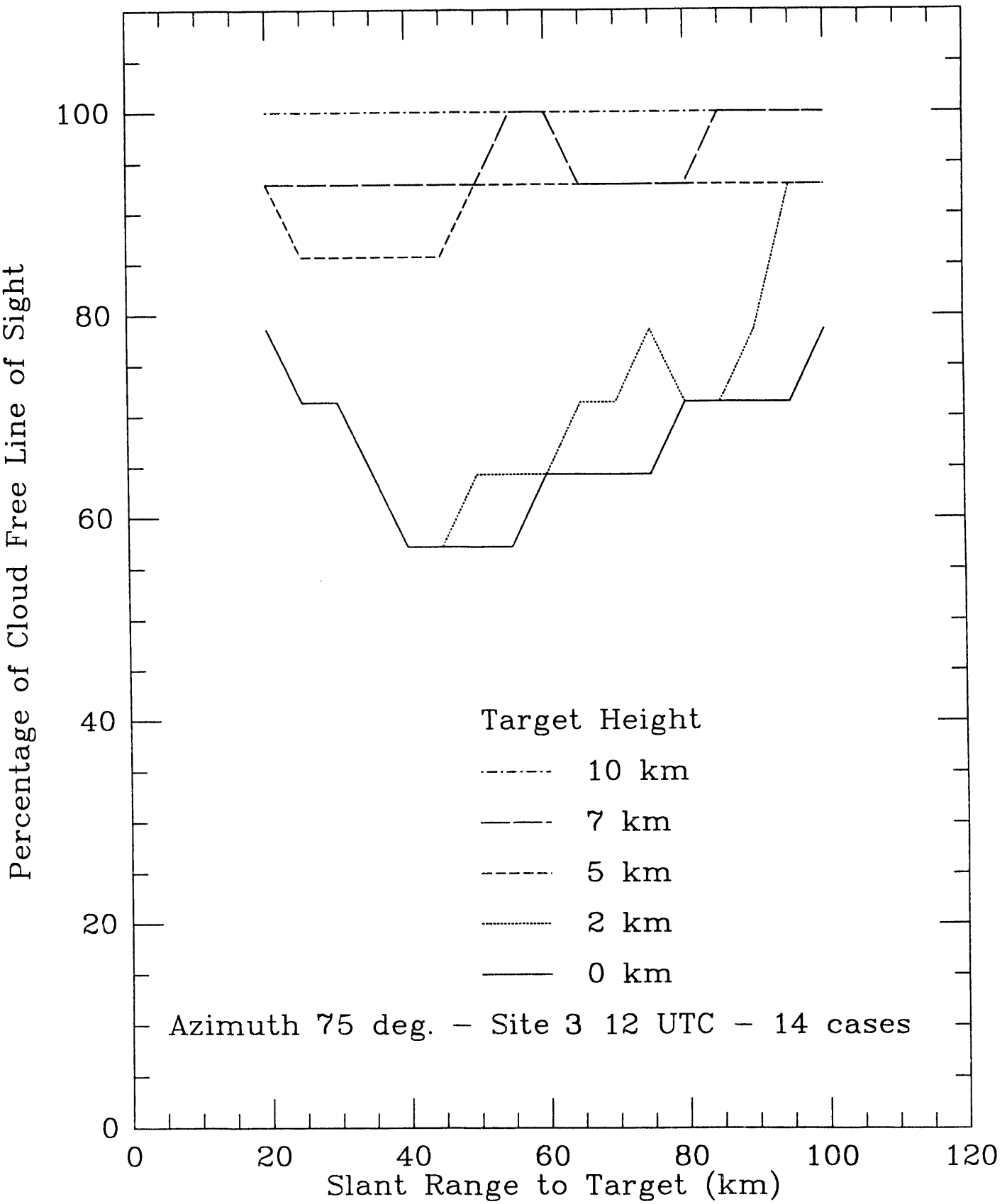
Percentage of Cloud Free Line of Sight
100
80
60
40
20
0
0
20
40
60
80
100
120
Slant Range to Target (km)
Target Height
10 km
7 km
5 km
2 km
0 km
Azimuth 75 deg. – Site 3 12 UTC – 14 cases

Figure 23.

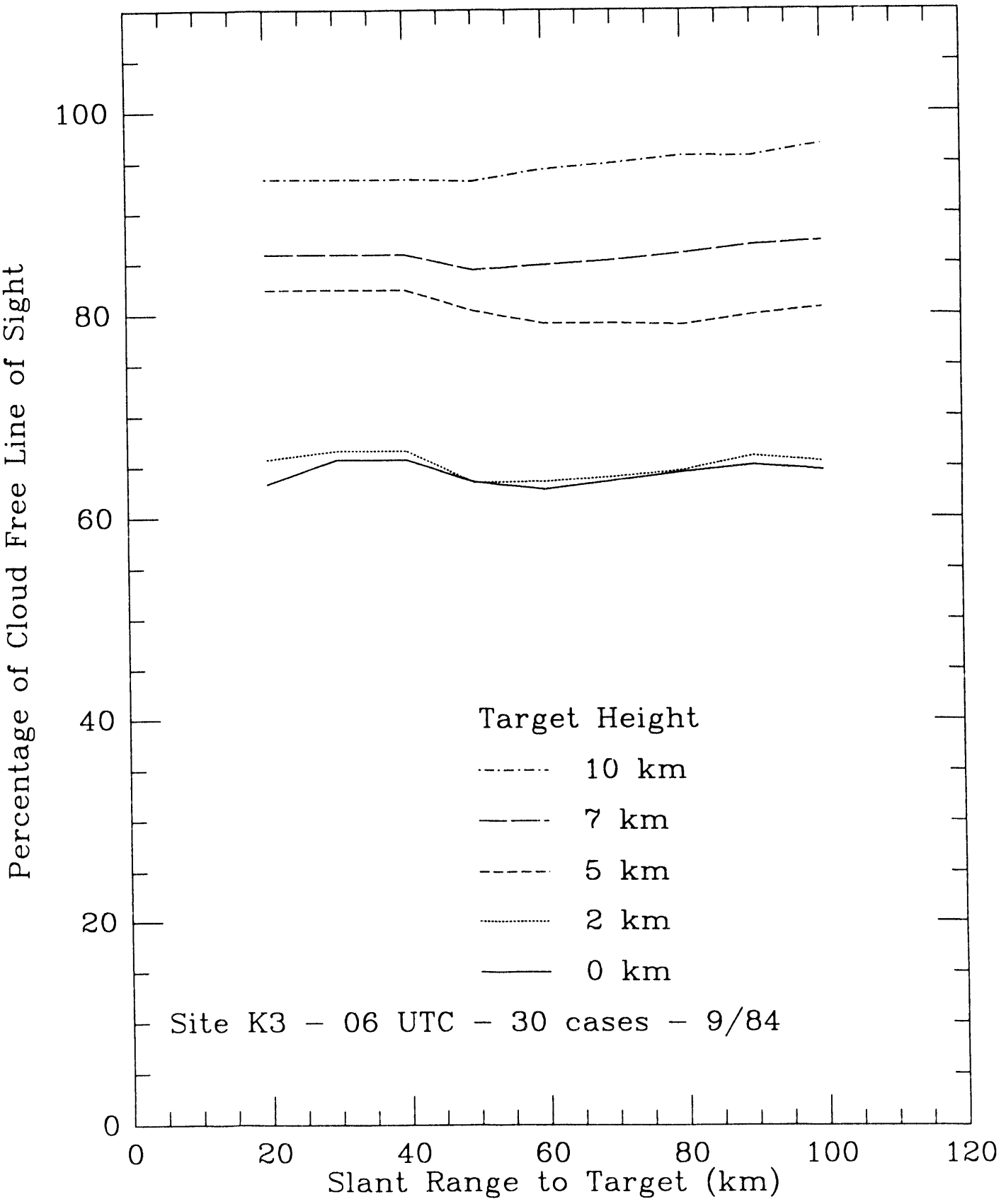
Percentage of Cloud Free Line of Sight
100
80
60
40
20
0
0
20
40
60
80
100
120
Slant Range to Target (km)
Target Height
10 km
7 km
5 km
2 km
0 km
Site K3 - 06 UTC - 30 cases - 9/84

Figure 24.

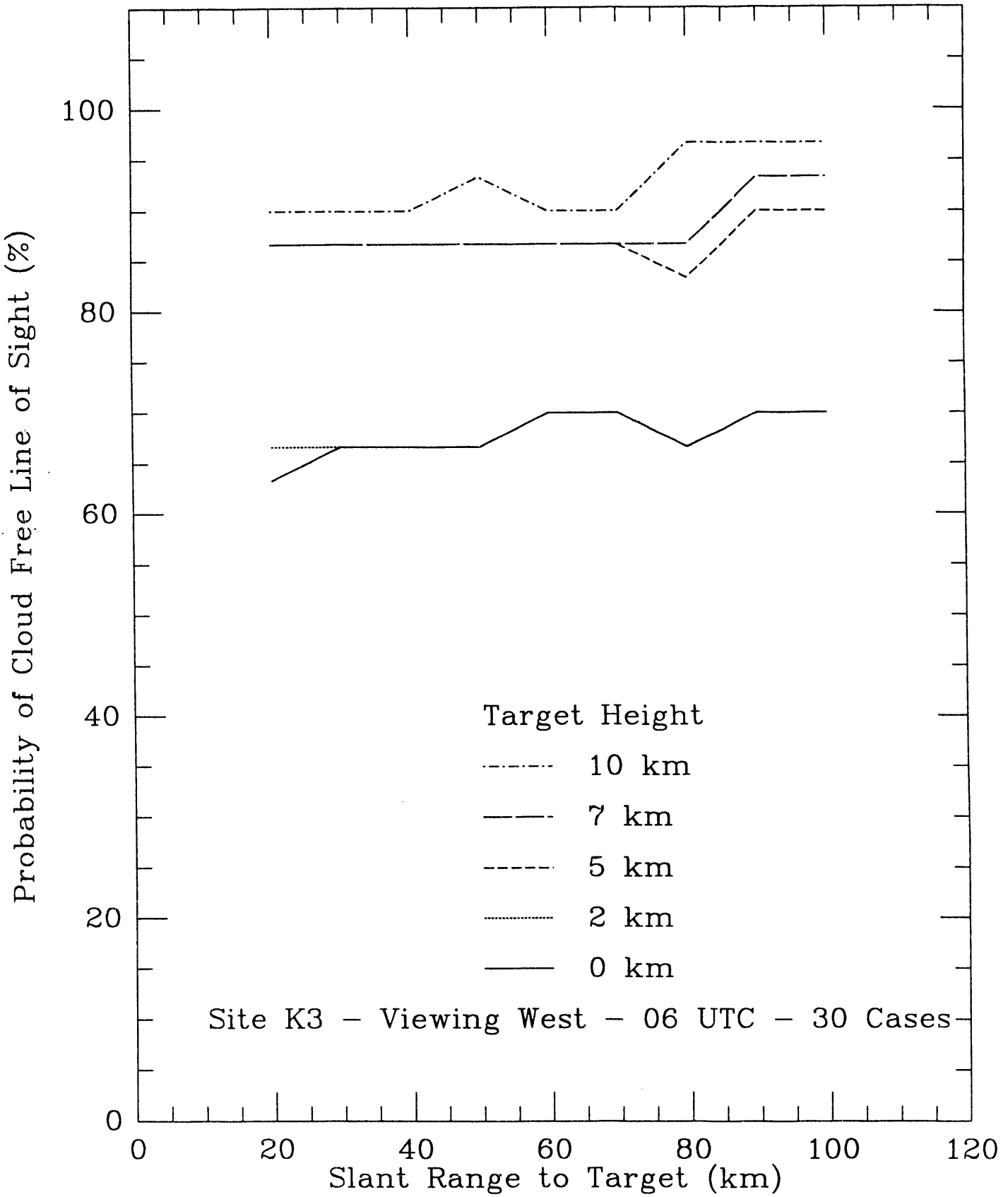
Probability of Cloud Free Line of Sight (%)
100
80
60
40
20
0
0
20
40
60
80
100
120
Slant Range to Target (km)
Target Height
10 km
7 km
5 km
2 km
0 km
Site K3 – Viewing West – 06 UTC – 30 Cases

Figure 25.

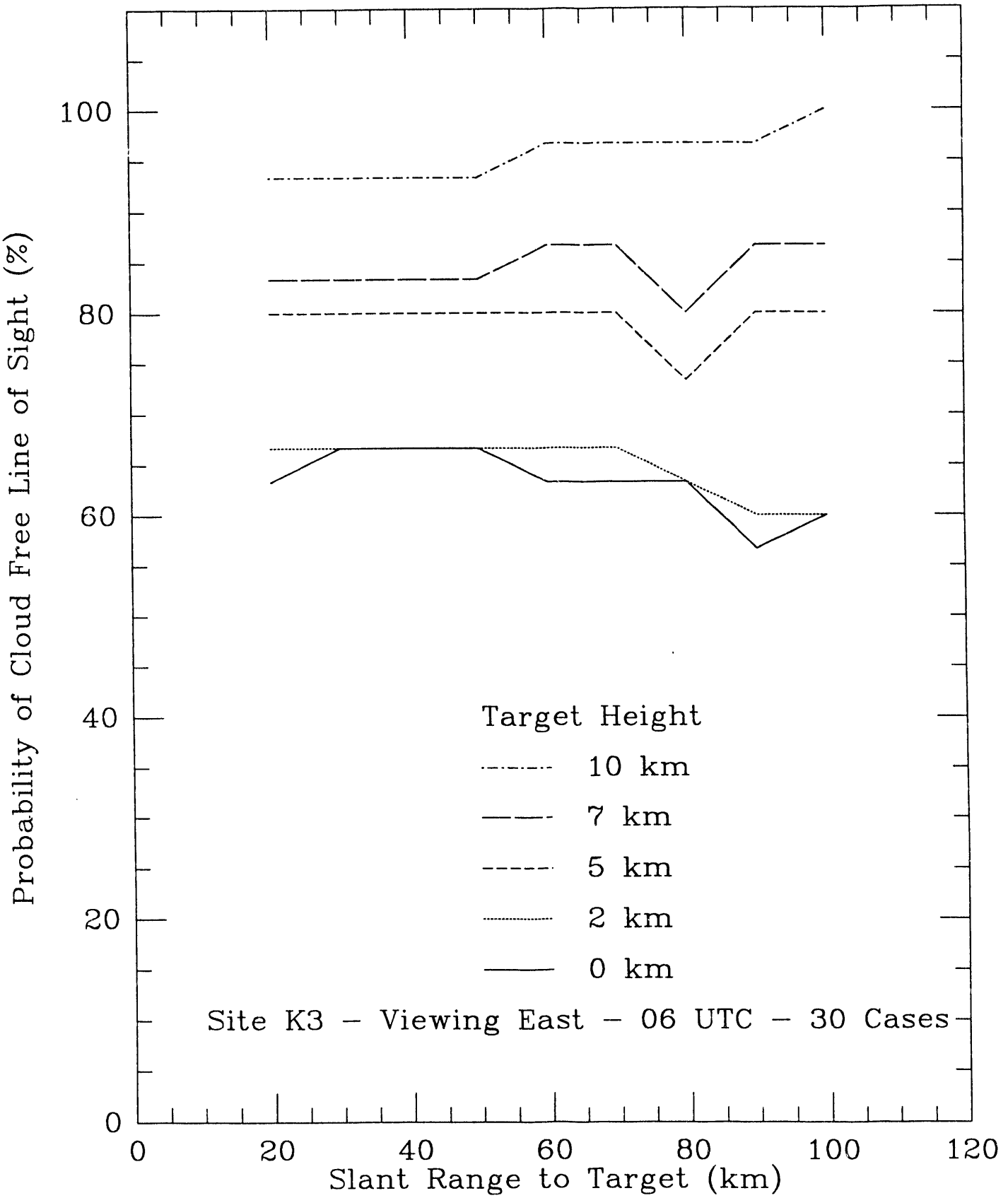
Probability of Cloud Free Line of Sight (%)
100
80
60
40
20
0
0
20
40
60
80
100
120
Slant Range to Target (km)
Target Height
10 km
7 km
5 km
2 km
0 km
Site K3 – Viewing East – 06 UTC – 30 Cases

Figure 26.

| | |
|---|---|
| Cloud base (m) | 3326.205 |
| Cloud base (m) | 2012.194 |
| Cloud base (m) | 2245.829 |
| Cloud base (m) | 2245.829 |
| Cloud base (m) | 1583.200 |
| Cloud base (m) | 2707.895 |
| Cloud base (m) | 2707.895 |
| Cloud base (m) | 1956.820 |
| Cloud base (m) | 1956.820 |
| Cloud base (m) | 2764.094 |
| Cloud base (m) | 2769.711 |
| Cloud base (m) | 2769.711 |
| Cloud base (m) | 2758.628 |
| Cloud base (m) | 2758.628 |
| Cloud base (m) | 2429.440 |
| Cloud base (m) | 1197.000 |
| Cloud base (m) | 2556.063 |
| Cloud base (m) | 1941.672 |
| Cloud base (m) | 2024.814 |
| Cloud base (m) | 2024.814 |
| Cloud base (m) | 2725.048 |
| Cloud base (m) | 2867.617 |
| Cloud base (m) | 2867.617 |
| Cloud base (m) | 2562.448 |
| Cloud base (m) | 2562.448 |
| Cloud base (m) | 3089.238 |
| Cloud base (m) | 3089.238 |
| Cloud base (m) | 2260.195 |

Table 2.

| | |
|---|---|
| Max cloud top (m) | 10640 |
| Max cloud top (m) | 11177 |
| Max cloud top (m) | 8107 |
| Max cloud top (m) | 2322 |
| Max cloud top (m) | 0 |
| Max cloud top (m) | 9811 |
| Max cloud top (m) | 7969 |
| Max cloud top (m) | 11558 |
| Max cloud top (m) | 3539 |
| Max cloud top (m) | 4715 |
| Max cloud top (m) | 3958 |
| Max cloud top (m) | 3284 |
| Max cloud top (m) | 5282 |
| Max cloud top (m) | 4110 |
| Max cloud top (m) | 16243 |
| Max cloud top (m) | 5268 |
| Max cloud top (m) | 9426 |
| Max cloud top (m) | 3215 |
| Max cloud top (m) | 4214 |
| Max cloud top (m) | 0 |
| Max cloud top (m) | 0 |
| Max cloud top (m) | 0 |
| Max cloud top (m) | 8051 |
| Max cloud top (m) | 10036 |
| Max cloud top (m) | 0 |
| Max cloud top (m) | 5186 |
| Max cloud top (m) | 7798 |
| Max cloud top (m) | 11817 |
| Max cloud top (m) | 0 |
| Max cloud top (m) | 0 |

Table 3.

| | |
|---|---|
| Cloud base (m) | 620.3989 |
| Cloud base (m) | 579.3287 |
| Cloud base (m) | 1344.431 |
| Cloud base (m) | 1327.182 |
| Cloud base (m) | 1529.031 |
| Cloud base (m) | 872.9227 |
| Cloud base (m) | 1248.975 |
| Cloud base (m) | 781.6648 |
| Cloud base (m) | 1245.159 |
| Cloud base (m) | 1564.039 |
| Cloud base (m) | 1370.366 |
| Cloud base (m) | 1377.909 |
| Cloud base (m) | 734.1902 |
| Cloud base (m) | 887.4487 |
| Cloud base (m) | 1317.789 |
| Cloud base (m) | 1408.477 |
| Cloud base (m) | 1353.294 |
| Cloud base (m) | 765.0334 |
| Cloud base (m) | 975.3895 |
| Cloud base (m) | 902.0278 |
| Cloud base (m) | 1493.474 |
| Cloud base (m) | 1271.027 |
| Cloud base (m) | 1326.529 |
| Cloud base (m) | 1105.512 |
| Cloud base (m) | 3025.207 |
| Cloud base (m) | 1694.748 |
| Cloud base (m) | 1018.729 |
| Cloud base (m) | 664.0807 |
| Cloud base (m) | 965.3822 |
| Cloud base (m) | 1820.899 |

Table 4.

## 8.0 BIBLIOGRAPHY


Kneizys, F.X., E.P. Shettle, L.W. Abreu, J.H. Chetwynd, G.P. Anderson, W.O. Gallery, J.E.A. Selby, and S.A. Clough, 1988: Users guide to LOWTRAN 7. Environmental Research Papers, No. 1010, Air Force Geophysics Laboratory, AFGL-TR-88-0177.

Liou, K.N., Y. Takano, S.C. Ou, A. Heymsfield, and W. Kreiss, 1990: Infrared transmission through cirrus clouds: a radiative model for target detection. *Applied Optics*, **29**, 1886-1896.

Sassen, K. and B.S. Cho, 1992: Subvisual--thin cirrus lidar dataset for satellite verification and climatological research. *J. of Applied Meteor.*, **31**, 1275-1285.

Snow, J.W., 1990: Modeling the variation of cloud cover with view angle using space shuttle cloud imagery. Environmental Research Papers, No. 1064, Geophysics Laboratory, GL-TR-90-0130.

Woodbury, G.E. and M.P. McCormick, 1986: Zonal and geographical distributions of cirrus clouds determined from SAGE data. *J. of Geophysical Research*, **91**, 2775-2785.

DATE
FILMED
10/27/93
END